Journal of Sound and Vibration 526 (2022) 116761

Contents lists available at ScienceDirect

Journal of Sound and Vibration

journal homepage: www.elsevier.com/locate/jsvi

Direct observation of edge modes in zigzag granular chains

Li-Yang Zheng [a,b,*], Shilin Qu [a], Florian Allein [a,c,**], Théo Thréard [a], Vitalyi Gusev [a], Vincent Tournat [a], Georgios Theocharis [a,***]

[a] Laboratoire d'Acoustique de l'Université du Mans (LAUM), UMR 6613, Institut d'Acoustique - Graduate School (IA-GS), CNRS, Le Mans Université, France

[b] School of Science, Shenzhen Campus of Sun Yat-sen University, Shenzhen, China

[c] Univ. Lille, CNRS, Centrale Lille, Univ. Polytechnique Hauts-de-France, Junia, UMR 8520 -IEMN, F-59000 Lille, France

ARTICLE INFO

Keywords:
Edge modes
Granular structures
Zigzag granular chain

ABSTRACT

As a new class of artificial elastic materials, granular crystals are mechanical structures of elastic beads arranged in contact through a lattice. One important feature of wave dynamics in granular crystals is that it highly relies on the contact mechanics, allowing for exotic wave transport properties such as rotational waves, solitary waves, slow edge waves, topological edge waves, etc. Realizing granular structures with well-predicted wave physics not only renders these new properties to mechanical systems, but provides also significant possibilities for advanced elastic wave control scenarios. Here, we theoretically and experimentally study the linear wave dynamics in one-dimensional (1D) zigzag granular chains constructed with macroscopic spherical stainless steel/tungsten beads. A spring–mass model including normal, shear and bending mechanical couplings between beads is proposed to characterize the wave dynamics in the chain, which turns out to exhibit remarkable agreement with the experimental measurements. Our work confirms the existence of localized translational–rotational coupled modes at the ends of granular chains, and it might motivate future studies for novel topological wave effects in granular structures.

1. Introduction

The exploration of periodic man-made structures has attracted considerable interest owing to their extraordinary abilities for advanced wave manipulation [1]. This recent, growing interest in artificial classical wave systems, including photonics [2,3], phononics [4,5], and mechanical structures [6,7], lies in the fact that various novel wave properties in electronic systems can be replicated in classical wave systems, which largely eases the challenges of experimental observation. In one dimensional (1D) periodic structures, zigzag chains have been intensively investigated. On one hand, zigzag chains exhibit a Dirac cone on the edges of the Brillouin zone due to the doubling of the unit cell. On the other hand, zigzag chains also hold nonsymmorphic symmetry, i.e., glide symmetry (a mirror combined with a half translation along the chain direction), that keeps the Dirac cone invariant no matter the angle of two sublattice sites. It has been shown that topological edge states can appear in dielectric zigzag arrays [8,9]. Moreover, when materials with gain are used, the topological edge states in such simple 1D zigzag arrays of micropillars can lead to topological lasing [10].

* Corresponding author at: School of Science, Shenzhen Campus of Sun Yat-sen University, Shenzhen, China.

** Corresponding author at: Univ. Lille, CNRS, Centrale Lille, Univ. Polytechnique Hauts-de-France, Junia, UMR 8520 -IEMN, F-59000 Lille, France.

*** Corresponding author at: Laboratoire d'Acoustique de l'Université du Mans (LAUM), UMR 6613, Institut d'Acoustique - Graduate School (IA-GS), CNRS, Le Mans Université, France.

E-mail addresses: zhengly27@mail.sysu.edu.cn (L.-Y. Zheng), florian.allein@junia.com (F. Allein), georgiostheocharis@gmail.com (G. Theocharis).

https://doi.org/10.1016/j.jsv.2022.116761
Received 31 May 2021; Received in revised form 17 December 2021; Accepted 10 January 2022
Available online 29 January 2022

Under this context, granular zigzag chains, spatially periodic structures of spherical elastic beads, potentially have even richer wave dynamics due to their multiple degrees of freedom. As had been theoretically and experimentally studied [11–14], in granular chains as well as in other granular structures, the beads are in direct contact through the contacting surfaces [15,16], which are of much smaller dimensions than the beads themselves. This leads to a very appealing property, that is, in addition to the predominant normal and shear interactions as in most of the mechanical systems, rotation of individual beads can be easily initiated by non-central shear forces, thus allowing for the propagation of rotational waves in the structures [17,18]. It has been shown that coupled rotational/transverse modes are experimentally observed in a three-dimensional granular crystal [17]. Another important property of granular chains is the tunability of wave dynamics from linear to strongly nonlinear regime, depending on the contact mechanism between beads [19]. This allows for the observation of various nonlinear phenomena including solitons [20,21], nonlinear waves [22–24] and breathers [25,26]. Those appealing properties can also lead to very intriguing localized/edge modes when boundaries are taken into account. For instance, in 2D granular structures, previous theoretical studies have shown that transversal–rotational edge modes [27], extreme slow edge modes [28], topological rotational waves [29,30], are predicted.

In this work, we theoretically and experimentally study the linear wave dynamics in two 1D zigzag granular chains (ZGCs): a monoatomic chain composed of purely spherical stainless steel beads and a diatomic one with alternating stainless steel and tungsten beads along the chain. The beads are precisely placed on the top of a fine-designed substrate, via a proper magnetic field used to induce precompression between beads. A theoretical model is proposed to capture the wave dynamics in the chains taking into account the normal, shear and bending mechanical couplings between elastic beads. We further analyze ZGCs of finite size with a fixed mechanical boundary at one end and a free boundary on the other end. We show that the theoretical predictions share very good agreement with our experimental results. Additionally, edge modes, for both monoatomic and diatomic ZGCs, are experimentally observed. Our work extends the theoretical study in Ref. [31], where localized modes for different boundaries of a linear array of monoatomic granular chain are analyzed. It also should be mentioned that in the previous study of dielectric zigzag structures in Refs. [8,9], the existence of topological edge states is due to the fact that polarizations of dielectric nanoparticles in a zigzag array are coupled. This coupling leads to nontrivial topological phase. In this work, the aforementioned edge modes in the ZGCs might also have nontrivial topology. We believe that the observation of localized transversal–rotational modes in the ZGCs in this work is a fundamental first step towards the realization of topological edge modes in granular crystals for future experimental investigation where symmetries are thoroughly analyzed.

2. Experimental set-up and modeling

The ZGC under consideration is depicted in Fig. 1(a), where stainless steel beads (diameter $d = 8$ mm, density $\rho = 7650$ kg/m^3, Young's modulus $E = 190$ GPa, and Poisson's ratio $\nu = 0.3$) are precisely arranged in a zigzag chain (the relative angle between the direction passing through the centers of two adjacent beads to the chain direction is 30°). Such a mechanically stable structure is constructed by applying an external magnetic field, which is induced by permanent cylindrical neodymium-alloy ($Nd_2Fe_{14}B$) magnets (remanent magnetization $B = 1.37$ T, diameter 6 mm, and length 13 mm) pinned in a substrate with a pre-designed zigzag configuration, see Fig. 1(b). In our sample fabrication process, the distance between two adjacent magnets is designed to be equal to the diameter of the bead. We placed the beads precisely on top of each magnet site (the centers of the bead and the magnet are in the same vertical level) such that a zigzag granular chain with point contact is formed as shown in Fig. 1(b). To stabilize the chain, the magnet polarization is flipped from one site to its neighboring sites. Under this zigzag magnetic field, the elastic beads are magnetized and attracted by their neighbors, resulting in nearly identical precompression force between two adjacent particles that stabilizes the structure (we only consider the nearest couplings as the next nearest forces are too weak). We further place a thin layer of rubber (thickness 1.5 mm) on top of the substrate. The use of soft rubber ensures a high impedance contrast between the granular chain and the substrate, thus reducing their mechanical coupling. In addition, the high viscoelasticity of the rubber significantly reduces the energy leakage in the rubber. Thus, not only the transmission of elastic waves into the substrate is prevented, but also the mechanical coupling between the chain and the substrate is largely minimized. Under these conditions, the mechanical coupling is extremely weak and only affects the wave dynamics at low frequencies (less than 300 Hz), which is much lower than the studied frequency. Therefore, the mechanical coupling between the beads and the substrate can be ignored, resulting in a stabilized free-standing ZGC. Such a design of granular structures using external magnetic field possesses incomparable advantages over conventional mechanical systems. On one hand, it offers mechanically stabilized structures while free-of-border constraints which can be designed to have different lattice configurations in one and two dimensions. On the other hand, the easily accessible tunability of precompression by changing the magnetic field renders remarkable flexibilities for the study of elastic waves and vibration with rich wave phemonena [12].

The experimental set-up is shown in Fig. 1(c). The driver, a bead fixed to a piezoelectric transducer (*Panametrics* V3052), can launch in-plane motion in the ZGC, see Fig. 1(d). Each bead in the structure possesses one out-of-plane rotation φ around the z-axis and two in-plane translations u and v along the $x-$ and $y-$axes, respectively. Two laser vibrometers, which are sensitive to changes in the optical path length only along the beam direction, are used to monitor the u and v displacement components, separately.

To theoretically model wave dynamics in the ZGC, the couplings between beads via their contacts are captured by spring–mass interactions as depicted in Fig. 2(a). Regarding the mechanical contact coupling between adjacent beads and the possible movements of individual particles, normal, shear and bending interactions can take place under the in-plane motion excitation, which are characterized by the effective rigidities K_N, K_S and K_B, respectively. Once precompression and particle material are given, K_N, K_S and K_B can be estimated by Hertzian contact mechanics [19,27], see Appendix A. In the ZGC, there are two different positions, in which sublattice A (B) is connected only to sublattice B (A). The normal n_β, shear s_β, and bending b_β spring elongations between

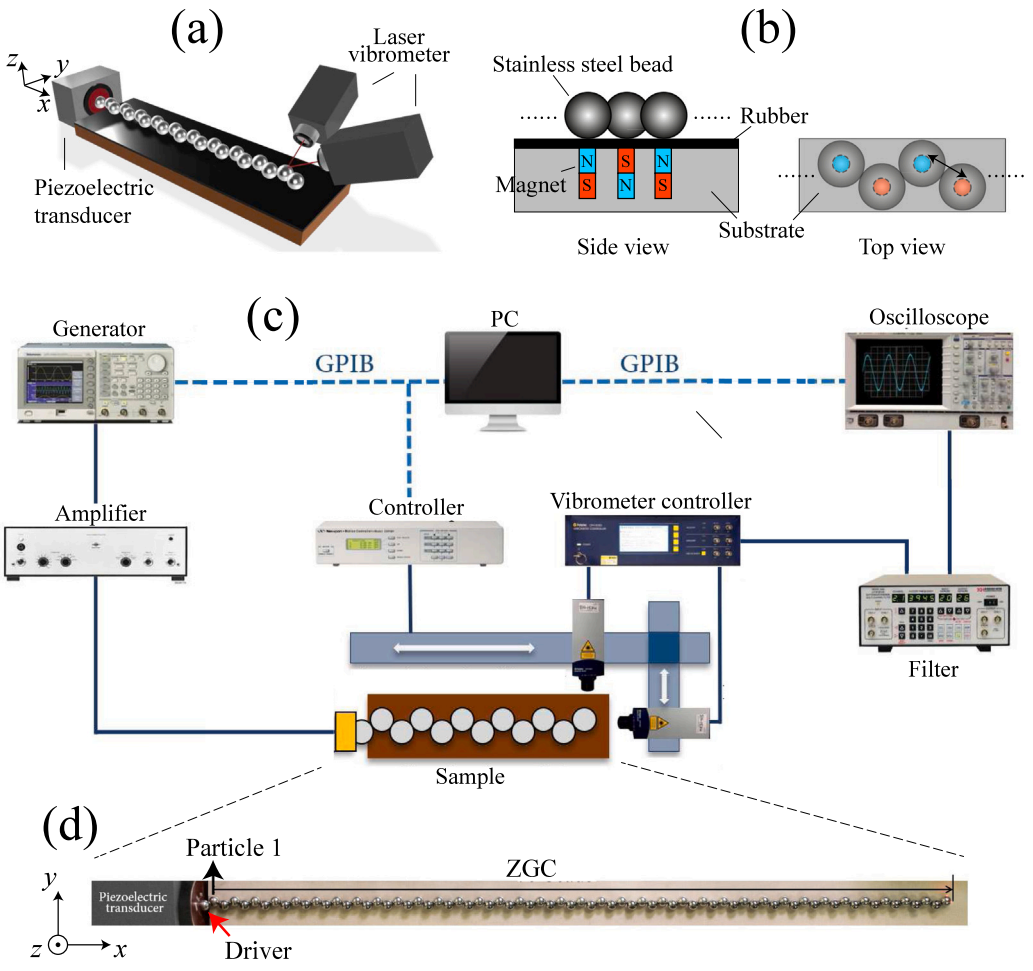

Fig. 1. Presentation of the zigzag granular chain (ZGC) and experimental set-up. (a) 3D view of the ZGC. (b) Side/top-view of the ZGC where the permanent magnets (red and blue) lead to attraction forces between the particles. (c) Experimental set-up. (d) A sample of the ZGC. (color required). (For interpretation of the references to color in this figure legend, the reader is referred to the web version of this article.)

adjacent beads, i.e., Fig. 2(a), can be expressed as,

$$n_\beta = (u_\beta - u_\alpha)\boldsymbol{e}_x\boldsymbol{e}_\beta + (v_\beta - v_\alpha)\boldsymbol{e}_y\boldsymbol{e}_\beta, \tag{1a}$$

$$s_\beta = (u_\beta - u_\alpha)\boldsymbol{e}_x\boldsymbol{l}_\beta + (v_\beta - v_\alpha)\boldsymbol{e}_y\boldsymbol{l}_\beta - \frac{d}{2}(\varphi_\beta + \varphi_\alpha), \tag{1b}$$

$$b_\beta = \frac{d}{2}(\varphi_\beta - \varphi_\alpha), \tag{1c}$$

where $\alpha = A, B$ is the sublattice index. $\beta = \pm$ is defined as a neighboring index since each sublattice is linked with its previous neighbor '–' and its next neighbor '+ ' as shown in Fig. 2(b). We define $\boldsymbol{e}_\beta$ as unit vectors in the directions from the center of α bead to the center of its β-th neighbors, see Fig. 2(b). $\boldsymbol{e}_x$, $\boldsymbol{e}_y$ and $\boldsymbol{e}_z$ represent the unit vectors along the $x-$, $y-$ and $z-$axes. $\boldsymbol{l}_\beta$ are unit vectors normal to $\boldsymbol{e}_\beta$ and $\boldsymbol{e}_z$ with the form $\boldsymbol{l}_\beta = \boldsymbol{e}_z \times \boldsymbol{e}_\beta$. Considering the nth α bead, denoted as α_{n}, the following equations of motion can be obtained by analyzing the interactions with its first neighbors,

$$M_\alpha \ddot{u}_{\alpha,\mathrm{n}} = \sum_\beta (K_N n_\beta \boldsymbol{e}_x\boldsymbol{e}_\beta + K_S s_\beta \boldsymbol{e}_x\boldsymbol{l}_\beta), \tag{2a}$$

$$M_\alpha \ddot{v}_{\alpha,\mathrm{n}} = \sum_\beta (K_N n_\beta \boldsymbol{e}_y\boldsymbol{e}_\beta + K_S s_\beta \boldsymbol{e}_y\boldsymbol{l}_\beta), \tag{2b}$$

$$I_\alpha \ddot{\varphi}_{\alpha,\mathrm{n}} = \frac{d}{2}\sum_\beta (K_S s_\beta + K_B b_\beta). \tag{2c}$$

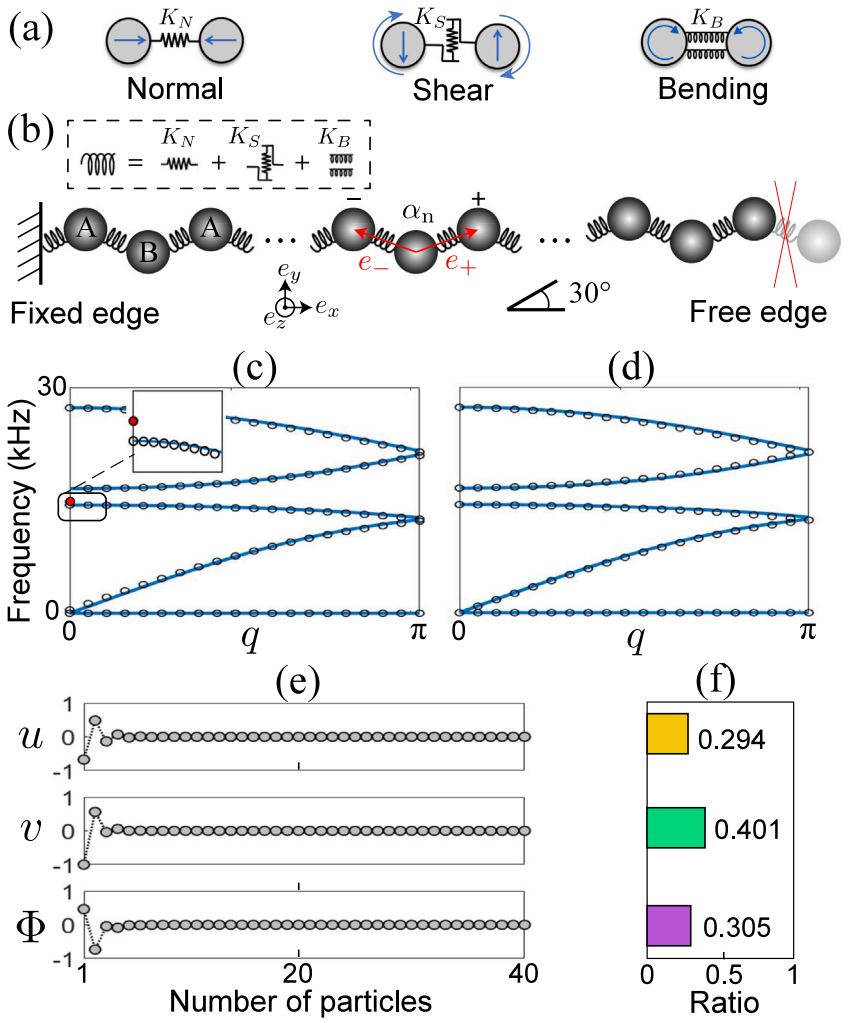

Fig. 2. (a) Considered mechanical couplings between beads in the ZGC. (b) The schematic presentation of the ZGC with fixed and free edges. The corresponding dispersion curves of a ZGC with 40 beads are presented in (c) for fixed–free edges, and in (d) for free–free edges. The inset is a close view of the edge mode (red) at the fixed edge. The near zero-frequency branches are due to the weak bending rigidity compared to shear and normal ones. (e) The eigenmode profile of the edge mode. u, v, Φ are normalized by the absolute value of the dominant component in a given mode. (f) Weights of each component in the edge mode. (color required). (For interpretation of the references to color in this figure legend, the reader is referred to the web version of this article.)

Above, M_α is the mass of the α bead and I_α is its moment of inertia. The dots on the top represent derivation over time. The products of unit vectors associated in Eqs. (2) are listed in Appendix B. Based on the equations of motion Eqs. (2), wave dynamics in the ZGC can be described by,

$$\mathcal{M}_A \ddot{\boldsymbol{U}}_{\mathrm{n}}^{A} = S_0 \boldsymbol{U}_{\mathrm{n}}^{A} + S_1 \boldsymbol{U}_{\mathrm{n}}^{B} + S_2 \boldsymbol{U}_{\mathrm{n-1}}^{B}, \tag{3a}$$

$$\mathcal{M}_B \ddot{\boldsymbol{U}}_{\mathrm{n}}^{B} = D_0 \boldsymbol{U}_{\mathrm{n}}^{B} + D_1 \boldsymbol{U}_{\mathrm{n}}^{A} + D_2 \boldsymbol{U}_{\mathrm{n+1}}^{A}, \tag{3b}$$

where $\boldsymbol{U}_{\mathrm{n}}^{\alpha} = [u_\alpha; v_\alpha; \boldsymbol{\Phi}_\alpha]_{\mathrm{n}}$ with $\boldsymbol{\Phi} = \varphi d/2$. $\mathcal{M}_\alpha = \mathrm{diag}[M_\alpha, M_\alpha, 4I_\alpha/d^2]$. S_i and D_i $(i = 0, 1, 2, 3)$ are 3×3 matrices, see Appendix C. By applying the Bloch periodic boundary conditions in the x-axis, i.e., $\boldsymbol{U}_{\mathrm{n}}^{\alpha} = \boldsymbol{U}^{\alpha} e^{i\omega t - iq\mathrm{n}}$ with the normalized wave vectors $q = \sqrt{3}kd/2$, Eqs. (3) can be mapped into an eigenvalue problem which leads to the dispersion curves of an infinite ZGC.

In experiment, the first bead of the ZGC is connected to the driver and the last bead is linked only to its '−' neighbor as shown in Fig. 2(b). The boundary condition of the first bead can be regarded as fixed edge because the driver is treated as a rigid "wall" with a huge mass compared to the beads in the ZGC. While on the other end of the chain, the last bead interacts with a smaller number of neighboring beads than in the volume. Thus, the boundary condition for the last bead can be characterized as a mechanically free edge obtained by removing its '+ ' neighbor. Analyzing the interactions on the first bead leads to the fixed boundary condition:

$$\boldsymbol{U}_{0}^{B} = 0. \tag{4}$$

In numerical simulation, an input signal can be arranged to $\boldsymbol{U}_0^B$ to mimic the driver as a 'moving' wall exciting in-plane motion in the ZGC. And for the last bead, the free boundary condition reads,

$$Q_0\boldsymbol{U}_{\mathrm{N}}^{\alpha} + Q_1\boldsymbol{U}^{+} = 0, \tag{5}$$

indicating the interactions of last bead N with its '+ ' neighbor are zero. Q_0 and Q_1 are 3×3 matrices, see Appendix C. Based on Eqs. (3)–(5), wave dynamics of a finite size ZGC can be unveiled. As examples, the dispersion relations of ZGC containing 40 identical particles with fixed–free and free–free boundaries are presented in Figs. 2(c) and 2(d), respectively. The curves marked by black circles belong to dispersion of the finite size ZGC, while the solid curves correspond to the infinite cases. Compared to the case of free boundary, an additional mode [red dot in the inset of Fig. 2(c)] is found at the fixed edge at around 15 kHz. The corresponding eigenmode is shown in Fig. 2(e), where the edge mode nature is found since the motion is highly confined near the fixed end, while decaying quickly into the chain. The weights of each component in the eigenmode are presented in Fig. 2(f), revealing that the mode is dominated by the v component. Thus this edge mode is potentially monitored in experiment by the laser vibrometer oriented in the y-axis. One might notice that there exists near zero-frequency branches in Figs. 2(c) and (d). The origin of the near zero-frequency branches has been investigated in Refs. [28,32]. The modes in these branches are mainly determined by bending interactions between beads. However, as the bending rigidity is much weaker than shear and normal ones in general, the bands become nearly flat and the corresponding modes are difficult to be excited. One should also notice that, the angle between beads can change the wave dynamics in the chain as well. This influence discussed in Appendix D can be studied in our theory based on Eqs. (2). In our experiment implementation, we focus on the case that the angle between beads is 30°.

3. Monoatomic zigzag granular chain

A narrow wave packet composed of a 16 kHz sine wave modulated by a gaussian function is launched from the generator as a source excitation in a monoatomic ZGC composed of 73 stainless steel beads. The v components of sublattice A are collected using the laser vibrometer. By scanning all the particles, the spatio-temporal signals of v component are obtained as presented in Fig. 3(b), where a reflection around $t = 2.8$ ms is observed. Using the same source signal, numerical simulations of the experiment can be implemented using Eqs. (3) together with the boundary conditions in Eqs. (4) and (5). However, dissipation has to be taken into account in order to mimic the real experimental process for elastic wave propagation. Regardless of the complex mechanism of dissipation involving frictions between beads, of the beads with the substrate and heat loss, etc., we found that the most significant damping in the granular chains is the on-site dissipation (this includes both dampings of the beads themselves and of the beads with the substrate) verified previously to have good agreement with numerical results and experiment [11,19,27]. Thus, a phenomenological on-site damping term is introduced to the right-hand side of Eqs. (3), $-1/\tau\dot{\boldsymbol{U}}_{\mathrm{n}}^{\alpha}$ with the coefficient τ, the decay time of waves, that is chosen by fitting the numerical results with experiment. In addition, based on previous studies in Refs. [12,19], where the precompression between two adjacent particles had been experimentally measured, we are able to estimate the precompression range, on the basis of which the precompression in this work can also be adjusted by means of simulations, leading to the accurate value with confidence. By setting precompression $\sim$2.4 N and damping $\tau \sim 0.4$ ms, the simulation of wave propagation in Fig. 3(a) has a good agreement with the experimental results. It also should be mentioned that in our experiment, each measurement is conducted with the same methodology, that is, the generator automatically sends the excitation signals 50 times and the laser vibrometer measures these 50 signals at each bead, and returns the average signals as measurement output. This allows us to obtain highly reliable results in experiment as will be presented in the following.

The dispersion relation of the ZGC can be obtained by applying Fourier transform of the spatio-temporal signals to the frequency–momentum q space. The simulated [measured] dispersion curves are shown in Fig. 3(c) [Fig. 3(d)]. The white lines in the background (dashed and solid) correspond to the theoretical modeling of an infinite chain. The color scale level reflects the intensity of v component in each mode. A good match between the experimental dispersion curves to both the theoretical and numerical ones is observed. However, compared to the theoretical results of an infinite chain, one additional mode around 15 kHz appears in both experiment and simulation of a finite ZGC. This mode corresponds to the edge mode at the fixed end as predicted in Fig. 2(c). To confirm, we re-implement the Fourier transform using the v data of sublattice A without the first two beads near the fixed end. The numerical and experimental results are demonstrated in Figs. 3(e) and 3(f), respectively, in which both show that the mode around 15 kHz disappears, verifying the edge mode nature as it is highly localized near the fixed end.

To shed more light on the fixed edge mode, we measure the frequency response of the 1st bead at the fixed end and the 73rd bead at the free end. A frequency sweep signal from 500 Hz to 30 kHz is launched. We monitor the v components of the two beads, and the corresponding frequency responses are shown in Fig. 3(g). It can be seen that there exists a peak around 15 kHz only for the first bead. We further show the v displacement distributions of the edge mode in Fig. 3(h). Both experiment and theory confirm the existence of the edge mode at $\sim$15 kHz at the fixed end of the ZGC. It should be mentioned that the frequency of the fixed edge mode can be shifted depending on the precompression force between the first bead and the driver (the effective rigidities among the two are modified in this case). This result is consistent with the analytic study in Ref. [31], where the frequency and mode shape of the localized modes are predicted to change for different boundary conditions.

The appearance of the fixed edge mode reported here might involve the topological property of the chain. Due to the multiple degrees of freedom in granular chains, there might be some hidden crystalline symmetries for the translation–rotation coupled modes which provide topological protection but are absent in conventional spring–mass chains without rotation. However, it is not straightforward to identify the topological origin based on conclusions from systems without rotation since translation and rotation are all coupled in granular chains. Thus, in this work, we focus on the theoretical, numerical and experimental tools for the observation of edge modes, while their topological properties will be no longer discussed.

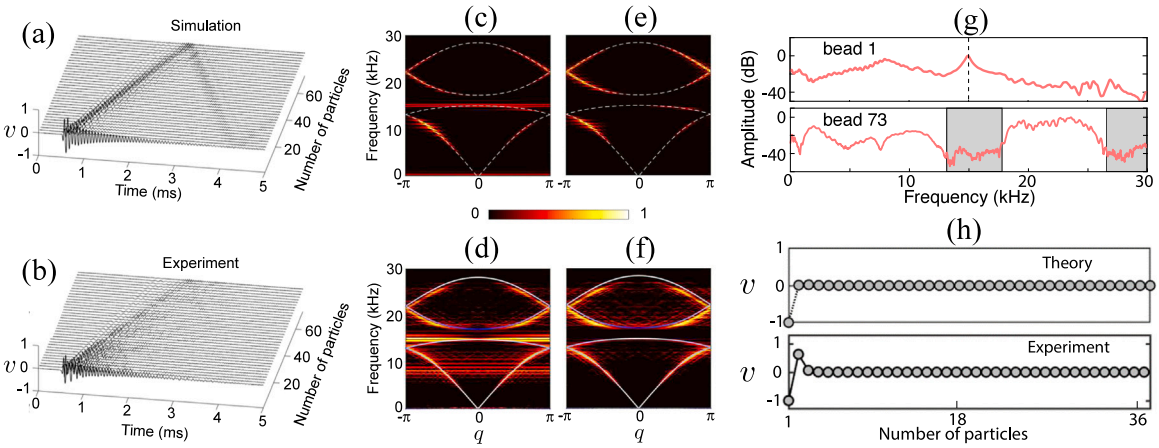

Fig. 3. A monoatomic chain consisting of 73 stainless steel beads. A bead glued to the piezoelectric transducer is used as the driver. (a), (b) Simulation and measurement of spatio-temporal signals of the v component in the sublattice A positions. (c)–(f) Dispersion curves obtained by numerical simulations in panels (c), (e), and by measurements in panels (d), (f). White dashed/solid lines correspond to the bulk bands from theoretical modeling. The color scale indicates the intensity of v component in each mode. (c), (d) Dispersion curves obtained using all the v data of sublattice A while panels (e), (f) are calculated without the first two beads near the fixed end. (g) Frequency response of the 1st and the 73rd bead. The gray regions mark the positions of stop bands for the bulk modes. The dashed line highlights the position of the edge mode at $\sim$ 15 kHz. (h) Edge mode profiles of sublattices A regarding the v component. (color required). (For interpretation of the references to color in this figure legend, the reader is referred to the web version of this article.)

4. Diatomic zigzag granular chain

By replacing the stainless steel beads at sublattice B position to the tungsten ones (d = 8 mm, ρ = 14920 kg/m^3, E = 630 GPa, Poisson's ratio ν = 0.21), a diatomic ZGC with fixed–free edges can be constructed, as shown in Fig. 4(a). The dispersion relation of the diatomic ZGCs containing 40 particles with fixed–free boundaries is compared to the infinite case in Figs. 4(b). The insets are a close view of the three edge modes (red dots) at the fixed edge. In addition, the weights of each component in each eigenmode are presented in Fig. 4(c), revealing that the two edge modes at lower frequency, ~8.75 kHz and ~11 kHz, are dominated by translational motion u and v, respectively. In contrast, the higher frequency fixed-edge mode, at ~16 kHz, is rotation dominated (Φ component).

In experiment, since the magnetized strength of tungsten beads is weaker than the stainless steel beads, the precompression in the diatomic chain is smaller compared to the monoatomic chain. To better stabilize the structure and avoid the influence of strong nonlinearity (the weaker precompression is, the stronger nonlinear effects are), we change the rubber layer to a translucent silicone sheet of 0.5 mm. On one hand, the silicone sheet also serves efficiently to reduce the mechanical coupling between the chain and the substrate. On the other hand, the beads are closer to the magnets due to the smaller thickness of the layer (1/3 compared to the rubber layer). Thus, the magnetization strength between beads is increased, so does the precompression in the chain. In addition, we notice that the structure is also more stable when the chain is ending by a stainless steel bead since its magnetization is higher. Thus, a diatomic ZGC of 41 beads is constructed (starting and ending by stainless steel beads). Following a similar procedure as that for the monoatomic chain, the precompression is estimated around ~0.28 N and the damping $\tau \sim 0.4$ ms. We should mention that ending the chain with a lighter mass leads to the presence of edge modes localized at the free boundary. However, since these modes are localized far from the driver and have a frequency within the bulk gap, we do not expect to excite them, and as a consequence we cannot measure them in the current setup configuration. Here, we focus only on the modes appearing at the fixed boundary closed to the driver.

Wave dynamics in the diatomic chain is studied by sending a frequency sweep ranging from 500 Hz to 22 kHz. We collect the signals of the u and v components of sublattice A using the two vibrometers. We implement Fourier-transform of the spatial signals to the q-space, then the dispersion curves of the finite diatomic chain are obtained. This process can also be numerically simulated using Eqs. (3) together with Eqs. (4) and Eqs. (5) by assuming the precompression ~0.28 N and the damping $\tau \sim 0.4$ ms. The results are shown in Fig. 5, where the dispersion curves obtained from the u and v components are presented in the color plots of Figs. 5(a) and 5(b), respectively. The color scale corresponds to the intensity of components in each mode. The top panels are the results of simulations and the bottom ones are the experiments. The white solid lines represent the theoretical band structure of an infinite chain calculated from Eqs. (3) with periodic boundary conditions. A very good match is seen among the experiments, simulations and theoretical predictions.

In the diatomic chain, there exist additional edge modes observed only in the band structure of the finite sized diatomic chain, i.e. the flat branches (white dashed) at ~8.75 kHz and ~11 kHz. These modes correspond to the edge modes localized at the fixed-end. We can notice that a flat branch corresponding to the third fixed-edge mode at ~16 kHz is weakly observed on Fig. 5(a) for the numerical results (u component). This mode is rotation dominated [see Fig. 5(c)] that cannot be captured by the laser vibrometers. However, the two translation-dominated edge modes are visible. By considering the boundary conditions in Eq. (4), the eigenmodes

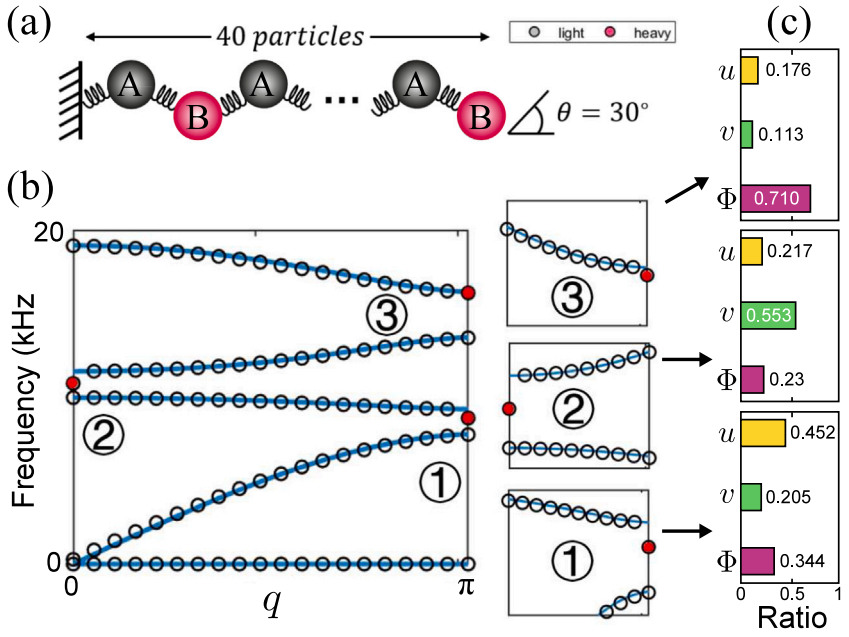

Fig. 4. (a) Schematic presentation of the diatomic ZGC with fixed–free edges. The light and heavy masses correspond to the stainless steel and tungsten particles, respectively. (b) Corresponding dispersion curves for a chain of 40 beads long (circle) and infinite chain (solid line) considering a precompression in the chain of 0.28 N. The insets are a close view of the three edge modes (red circle) at the fixed edge. (c) Weights of each component in the edge mode. (color required). (For interpretation of the references to color in this figure legend, the reader is referred to the web version of this article.)

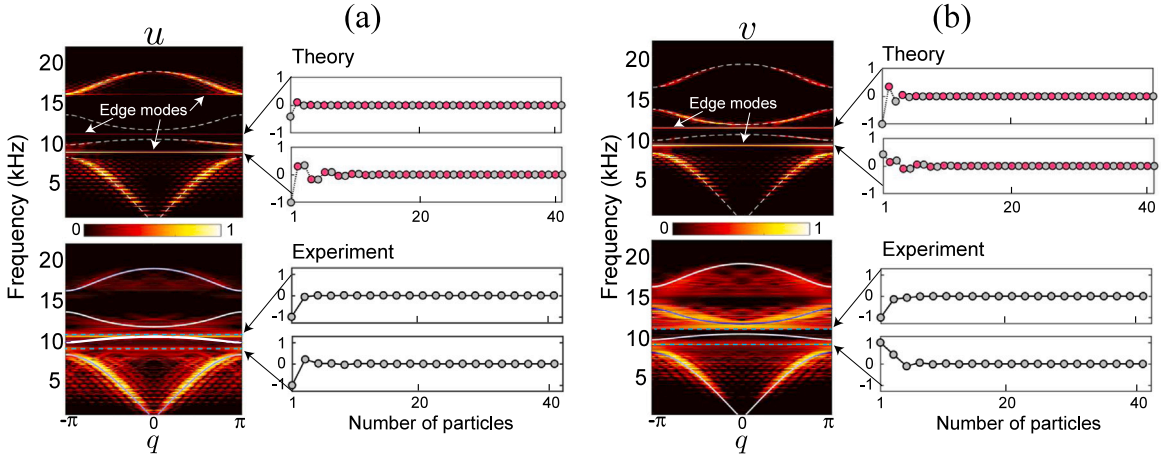

Fig. 5. Dispersion curves obtained by Fourier transforming the u component in (a) and the v component in (b). The edge mode profiles of each component in the diatomic ZGC are also shown in (a) and (b). Top (bottom) panels are the theoretical (experimental) results. White lines correspond to the bulk bands from theoretical modeling. The color scale indicates the intensity of modes. Two edge modes at ~8.75 kHz and ~11 kHz are observed. (color required). (For interpretation of the references to color in this figure legend, the reader is referred to the web version of this article.)

of the two edge modes can be obtained as shown in Figs. 5(a),(b) for the distribution of the u and v components, respectively. The beads in gray (magenta) are sublattices A (B). The measured edge mode profiles are also presented in Fig. 5 by detecting the displacement at ~8.75 kHz and ~11 kHz. The consistence between experiment and theory confirms the existence of the edge modes at the fixed end of the diatomic chain.

5. Conclusions

In this work, we studied the elastic wave properties in 1D zigzag granular chains. The dispersion curves for both monoatomic and diatomic chains have been measured. Moreover, we investigated the edge mode properties when boundaries appear. Direct observations of edge modes at the fixed boundary have been reported theoretically and experimentally. We believe that our results

in the 1D zigzag granular chains offer opportunities for experimental investigation of exotic wave phenomena such as topological edge/corner modes in granular systems, taking advantage of the unique features of granular systems such as rotational/rotational–translational modes. The proposed granular systems herein offers a perfect platform to explore complex wave dynamics including nonlinearity, leading to potential applications for mitigation, vibration damping, and energy harvesting.

CRediT authorship contribution statement

Li-Yang Zheng: Software, Conceptualization, Methodology, Writing – original draft, Formal analysis. **Shilin Qu:** Data curation, Investigation, Validation. **Florian Allein:** Visualization, Methodology, Writing – original draft, Formal analysis. **Théo Thréard:** Data curation, Investigation, Validation. **Vitalyi Gusev:** Methodology, Formal analysis. **Vincent Tournat:** Supervision, Formal analysis. **Georgios Theocharis:** Writing – review & editing, Supervision, Funding acquisition.

Declaration of competing interest

The authors declare that they have no known competing financial interests or personal relationships that could have appeared to influence the work reported in this paper.

Acknowledgments

G. T. acknowledges the support from the project CS.MICRO funded under the program Etoiles Montantes of the Region Pays de la Loire, France.

Appendix A. Contact rigidities

The schematics of the Hertzian contact under normal static load F_0 and a tangential force T_0 is presented in Fig. A1. First of all, considering only normal forces, F_0, directed along the centers of the two different beads (different radius and material), the radius of the contact surface, r_c, between two spheres can be expressed as:

$$r_c = \left(\frac{3F_0R^*}{4E^*}\right)^{1/3}, \tag{A.1}$$

where

$$\frac{1}{R^*} = \frac{1}{R_1} + \frac{1}{R_2} = \frac{R_1+R_2}{R_1R_2}, \text{ and } \frac{1}{E^*} = \frac{(1-\nu_1^2)}{E_1} + \frac{(1-\nu_2^2)}{E_2}, \tag{A.2}$$

with

F_0 : static force applied longitudinally on the spheres [N],
E_n : Young's modulus of each material [Pa],
ν_n : Poisson's ratio of each material,
R_n : radius of each sphere [m].

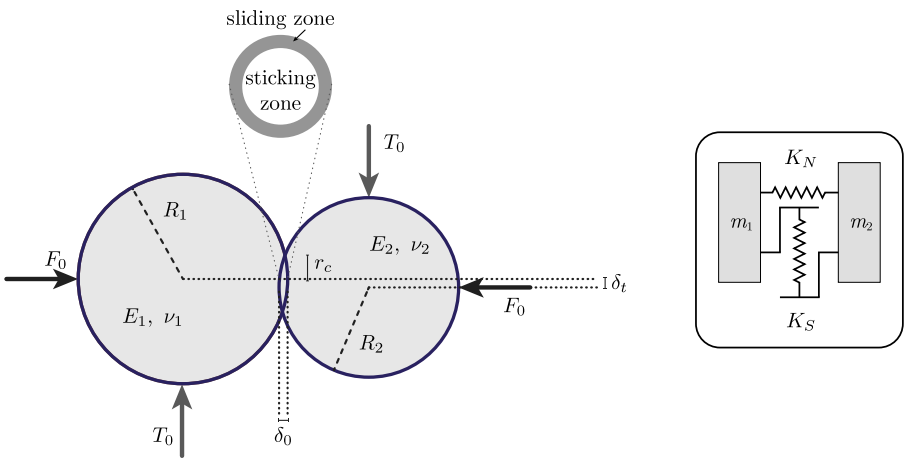

Fig. A1. Schematics of the contact between two spheres with a representation of the contact surface which depicts the phenomenon of stick/slip. The inset shows the linearized problem allowing a modeling of the system by two masses linked by two springs.

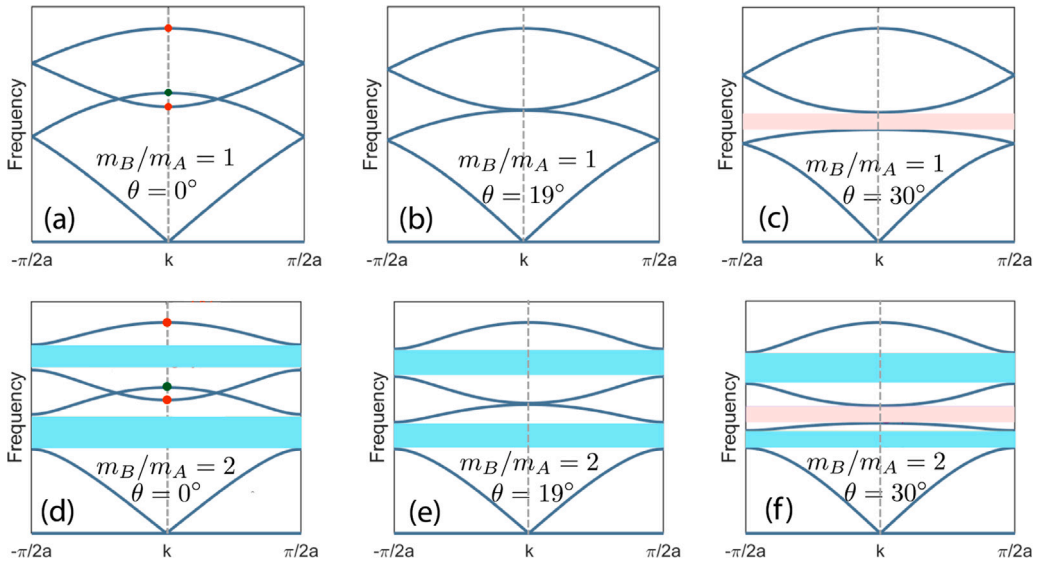

Fig. A2. Dispersion curves of monoatomic granular chain with the relative angle between particles in (a) $\theta = 0°$, (b) $\theta = 19°$, (c) $\theta = 30°$. (d), (e), (f) are the same angles as (a), (b), (c) but in a diatomic zigzag chain with mass ratio $m_B/m_A = 2$.

The relation between the applied normal force F_0 and the relative axial displacement δ_0 of the particles is written as:

$$\delta_0 = \frac{r_c^2}{R^*} = \left(\frac{F_0}{A}\right)^{2/3} = \left(\frac{9F_0^2}{16R^*E^{*2}}\right)^{1/3}, \tag{A.3}$$

and the coefficient A is given for two spheres as:

$$A = \frac{4E_1E_2\sqrt{\frac{R_1R_2}{R_1+R_2}}}{3E_2(1-\nu_1^2)+3E_1(1-\nu_2^2)}. \tag{A.4}$$

Finally, the normal interactions can be expressed as the normal stiffness K_N:

$$K_N = \frac{3}{2}A\delta_0^{1/2}. \tag{A.5}$$

The transversal interactions can be expressed as the shear stiffness K_S:

$$K_S = 2G^*r_c, \tag{A.6}$$

where G^* is the normalized shear modulus:

$$\frac{1}{G^*} = \frac{(2-\nu_1)}{4G_1} + \frac{(2-\nu_2)}{4G_2}, \tag{A.7}$$

and $G_1 = \frac{E_1}{2(1+\nu_1)}$ and $G_2 = \frac{E_2}{2(1+\nu_2)}$ are the shear modulus of each material.

The bending stiffness K_B can be expressed as:

$$K_B = K_N\frac{r_c}{R^*}. \tag{A.8}$$

For the monoatomic case with the precompression of 2.4 N presented in this paper, the stiffnesses are $K_N \approx 6.8\times10^6$, $K_S \approx 5.6\times10^6$, and $K_B \approx 4.8\times10^2$ expressed in N/m. For the diatomic case with the precompression of 0.28 N, $K_N \approx 4.4\times10^6$, $K_S \approx 3.6\times10^6$, and $K_B \approx 2.1\times10^2$ expressed in N/m.

Appendix B. Products of unit vectors

The unit vectors associated in the derivations of equation of motion are defined as $\boldsymbol{e}_x = (1,0,0), \boldsymbol{e}_y = (0,1,0), \boldsymbol{e}_z = (0,0,1)$. The directional vectors of two neighboring beads are given by $\boldsymbol{e}_+ = (\frac{\sqrt{3}}{2},\frac{1}{2},0), \boldsymbol{e}_- = (-\frac{\sqrt{3}}{2},\frac{1}{2},0)$ and $\boldsymbol{l}_+ = (-\frac{1}{2},\frac{\sqrt{3}}{2},0), \boldsymbol{l}_- = (-\frac{1}{2},-\frac{\sqrt{3}}{2},0)$ when the center bead is sublattice A. While $\boldsymbol{e}_+ = (\frac{\sqrt{3}}{2},-\frac{1}{2},0), \boldsymbol{e}_- = (-\frac{\sqrt{3}}{2},-\frac{1}{2},0)$ and $\boldsymbol{l}_+ = (\frac{1}{2},\frac{\sqrt{3}}{2},0), \boldsymbol{l}_- = (\frac{1}{2},-\frac{\sqrt{3}}{2},0)$ for sublattice B. The products of different unit vectors are listed in Tables 1 and 2 .

Table 1
Products for sublattice A.

	e_+	e_-	l_+	l_-
e_x	$\sqrt{3}/2$	$-\sqrt{3}/2$	$-1/2$	$-1/2$
e_y	$1/2$	$1/2$	$\sqrt{3}/2$	$-\sqrt{3}/2$

Table 2
Products for sublattice B.

	e_+	e_-	l_+	l_-
e_x	$\sqrt{3}/2$	$-\sqrt{3}/2$	$1/2$	$1/2$
e_y	$-1/2$	$-1/2$	$\sqrt{3}/2$	$-\sqrt{3}/2$

Appendix C. Dynamical matrices

Following the derivation for Eq. (3) in the main text, we can obtain the specific forms of each matrices:

$$S_0 = \begin{bmatrix} -\frac{K_S+3K_N}{2} & 0 & -K_S \\ 0 & -\frac{K_N+3K_S}{2} & 0 \\ -K_S & 0 & -2(K_S+K_N) \end{bmatrix}, \tag{A.9}$$

$$S_1 = \begin{bmatrix} \frac{K_S+3K_N}{4} & \frac{\sqrt{3}(K_N-K_S)}{4} & -\frac{K_S}{2} \\ \frac{\sqrt{3}(K_N-K_S)}{4} & \frac{K_N+3K_S}{4} & \frac{\sqrt{3}K_S}{2} \\ \frac{K_S}{2} & -\frac{\sqrt{3}K_S}{2} & K_B-K_S \end{bmatrix}, \tag{A.10}$$

$$S_2 = \begin{bmatrix} \frac{K_S+3K_N}{4} & \frac{\sqrt{3}(K_S-K_N)}{4} & -\frac{K_S}{2} \\ \frac{\sqrt{3}(K_S-K_N)}{4} & \frac{K_N+3K_S}{4} & -\frac{\sqrt{3}K_S}{2} \\ \frac{K_S}{2} & \frac{\sqrt{3}K_S}{2} & K_B-K_S \end{bmatrix}, \tag{A.11}$$

$$D_0 = \begin{bmatrix} -\frac{K_S+3K_N}{2} & 0 & K_S \\ 0 & -\frac{K_N+3K_S}{2} & 0 \\ K_S & 0 & -2(K_S+K_N) \end{bmatrix}. \tag{A.12}$$

$D_1 = S_1^{\mathrm{T}}$ and $D_2 = S_2^{\mathrm{T}}$ with T representing the transpose. For the free edge of the chains, the boundary condition can be obtained by removing the interaction of the last bead with its + neighbor. Considering the case where the last bead belongs to the sublattice A position, this leads to Eq. (5) in the main text where Q_0 is of the following form:

$$Q_0 = \begin{bmatrix} -\frac{K_S+3K_N}{4} & \frac{\sqrt{3}(K_S-K_N)}{4} & -\frac{K_S}{2} \\ \frac{\sqrt{3}(K_S-K_N)}{4} & -\frac{K_N+3K_S}{4} & \frac{\sqrt{3}K_S}{2} \\ -\frac{K_S}{2} & \frac{\sqrt{3}K_S}{2} & -K_B-K_S \end{bmatrix}, \tag{A.13}$$

and $Q_1 = S_1$.

Appendix D. Angle dependence on dispersion curves

In our granular chains, one can also change the relative angle θ between beads to tune the dynamic response. Based on the equations of motion in Eqs. (3), we can study the influence of different angle in the ZGCs. To demonstrate this, we show the dispersion curves of a monoatomic chain with $\theta = 0°, 19°, 30°$ in Fig. A2(a)–(c), and the ones of a diatomic chain with $\theta = 0°, 19°, 30°$ in Fig. A2(d)–(f). As can be seen in both monoatomic and diatomic ZGCs, increasing the angle θ leads to a tendency of shifting the second bulk band to low frequency while the third band to high frequency. At $\theta = 19°$, a transition occurs, beyond which a band gap (pink) appears between the second and the third bands. It should be noticed that, there are two additional gaps in the diatomic ZGC (cyan). These two gaps originate from the breaking of sublattice symmetry in the ZGC. Thus, tuning the angle θ cannot lead to the closing of this two gaps.

References

[1] M. Kadic, G.W. Milton, M. van Hecke, M. Wegener, 3D metamaterials, Nat. Rev. Phys. 1 (3) (2019) 198–210.
[2] M.H. Javani, M.I. Stockman, Real and imaginary properties of epsilon-near-zero materials, Phys. Rev. Lett. 117 (10) (2016) 107404.
[3] L. Ferrari, C. Wu, D. Lepage, X. Zhang, Z. Liu, Hyperbolic metamaterials and their applications, Prog. Quantum Electron. 40 (2015) 1–40.
[4] H. Ge, M. Yang, C. Ma, M.-H. Lu, Y.-F. Chen, N. Fang, P. Sheng, Breaking the barriers: advances in acoustic functional materials, Natl. Sci. Rev. 5 (2) (2018) 159–182.
[5] P. Gao, D. Torrent, F. Cervera, P. San-Jose, J. Sánchez-Dehesa, J. Christensen, Majorana-like zero modes in kekulé distorted sonic lattices, Phys. Rev. Lett. 123 (19) (2019) 196601.
[6] K. Bertoldi, V. Vitelli, J. Christensen, M. Van Hecke, Flexible mechanical metamaterials, Nat. Rev. Mater. 2 (11) (2017) 1–11.
[7] C. Kane, T. Lubensky, Topological boundary modes in isostatic lattices, Nat. Phys. 10 (1) (2014) 39–45.
[8] A.P. Slobozhanyuk, A.N. Poddubny, A.E. Miroshnichenko, P.A. Belov, Y.S. Kivshar, Subwavelength topological edge states in optically resonant dielectric structures, Phys. Rev. Lett. 114 (2015) 123901, http://dx.doi.org/10.1103/PhysRevLett.114.123901, URL https://link.aps.org/doi/10.1103/PhysRevLett.114.123901.
[9] S. Kruk, A. Slobozhanyuk, D. Denkova, A. Poddubny, I. Kravchenko, A. Miroshnichenko, D. Neshev, Y. Kivshar, Edge states and topological phase transitions in chains of dielectric nanoparticles, Small 13 (11) (2017) 1603190, http://dx.doi.org/10.1002/smll.201603190, URL https://onlinelibrary.wiley.com/doi/abs/10.1002/smll.201603190.
[10] P. St-Jean, V. Goblot, E. Galopin, A. Lemaître, T. Ozawa, L. Le Gratiet, I. Sagnes, J. Bloch, A. Amo, Lasing in topological edge states of a one-dimensional lattice, Nat. Photonics 11 (10) (2017) 651–656.
[11] N. Boechler, G. Theocharis, C. Daraio, Bifurcation-based acoustic switching and rectification, Nature Mater. 10 (9) (2011) 665–668.
[12] F. Allein, V. Tournat, V. Gusev, G. Theocharis, Tunable magneto-granular phononic crystals, Appl. Phys. Lett. 108 (16) (2016) 161903.
[13] E. Herbold, V. Nesterenko, Shock wave structure in a strongly nonlinear lattice with viscous dissipation, Phys. Rev. E 75 (2) (2007) 021304.
[14] E.G. Charalampidis, F. Li, C. Chong, J. Yang, P.G. Kevrekidis, Time-periodic solutions of driven-damped trimer granular crystals, Math. Probl. Eng. (2015).
[15] K.L. Johnson, Contact Mechanics, Cambridge University Press, 1987.
[16] R.D. Mindlin, Compliance of elastic bodies in contact, J. Appl. Mech. ASME 16 (1949) 259–268.
[17] A. Merkel, V. Tournat, V. Gusev, Experimental evidence of rotational elastic waves in granular phononic crystals, Phys. Rev. Lett. 107 (22) (2011) 225502.
[18] H. Pichard, A. Duclos, J.-P. Groby, V. Tournat, L. Zheng, V. Gusev, Surface waves in granular phononic crystals, Phys. Rev. E 93 (2) (2016) 023008.
[19] F. Allein, V. Tournat, V. Gusev, G. Theocharis, Linear and nonlinear elastic waves in magnetogranular chains, Phys. Rev. Appl. 13 (2) (2020) 024023.
[20] S. Job, F. Melo, A. Sokolow, S. Sen, How hertzian solitary waves interact with boundaries in a 1d granular medium, Phys. Rev. Lett. 94 (17) (2005) 178002.
[21] C. Chong, M.A. Porter, P.G. Kevrekidis, C. Daraio, Nonlinear coherent structures in granular crystals, J. Phys.: Condens. Matter 29 (41) (2017) 413003.
[22] A. Leonard, F. Fraternali, C. Daraio, Directional wave propagation in a highly nonlinear square packing of spheres, Exp. Mech. 53 (3) (2013) 327–337.
[23] A. Leonard, C. Daraio, Stress wave anisotropy in centered square highly nonlinear granular systems, Phys. Rev. Lett. 108 (21) (2012) 214301.
[24] J. Cabaret, P. Béquin, G. Theocharis, V. Andreev, V. Gusev, V. Tournat, Nonlinear hysteretic torsional waves, Phys. Rev. Lett. 115 (5) (2015) 054301.
[25] N. Boechler, G. Theocharis, S. Job, P. Kevrekidis, M.A. Porter, C. Daraio, Discrete breathers in one-dimensional diatomic granular crystals, Phys. Rev. Lett. 104 (24) (2010) 244302.
[26] G. Theocharis, M. Kavousanakis, P. Kevrekidis, C. Daraio, M.A. Porter, I. Kevrekidis, Localized breathing modes in granular crystals with defects, Phys. Rev. E 80 (6) (2009) 066601.
[27] L.-Y. Zheng, F. Allein, V. Tournat, V. Gusev, G. Theocharis, Granular graphene: Direct observation of edge states on zigzag and armchair boundaries, Phys. Rev. B 99 (18) (2019) 184113.
[28] L.-Y. Zheng, V. Tournat, V. Gusev, Zero-frequency and extremely slow elastic edge waves in mechanical granular graphene, Extrem. Mech. Lett. 12 (2017) 55–64.
[29] L.-Y. Zheng, G. Theocharis, V. Tournat, V. Gusev, Quasitopological rotational waves in mechanical granular graphene, Phys. Rev. B 97 (6) (2018) 060101.
[30] L.-Y. Zheng, G. Theocharis, R. Fleury, V. Tournat, V. Gusev, Tilted double dirac cone and anisotropic quantum-spin-hall topological insulator in mechanical granular graphene, New J. Phys. 22 (10) (2020) 103012.
[31] H. Pichard, A. Duclos, J.-P. Groby, V. Tournat, V.E. Gusev, Localized transversal-rotational modes in linear chains of equal masses, Phys. Rev. E 89 (2014) 013201, http://dx.doi.org/10.1103/PhysRevE.89.013201, URL https://link.aps.org/doi/10.1103/PhysRevE.89.013201.
[32] L.-Y. Zheng, H. Pichard, V. Tournat, G. Theocharis, V. Gusev, Zero-frequency and slow elastic modes in phononic monolayer granular membranes, Ultrasonics 69 (2016) 201–214.